Full Text View

Volume 28, Issue 7 (July 1998)

Journal of Physical Oceanography
Article: pp. 1425–1438 | Abstract | PDF (978K)

Observation of Short Wind Waves in Coastal Waters*

Tetsu Hara

Graduate School of Oceanography, University of Rhode Island, Narragansett, Rhode Island

Erik J. Bock, James B. Edson, and Wade R. McGillis

Department of Applied Ocean Physics and Engineering, Woods Hole Oceanographic Institution, Woods Hole, Massachusetts

(Manuscript received February 24, 1997, in final form September 18, 1997)

DOI: 10.1175/1520-0485(1998)028<1425:OOSWWI>2.0.CO;2

ABSTRACT

Observations of wind-generated gravity–capillary waves have been made during two recent field programs in coastal environments. The results of wave slope spectra on clean water show a well-defined correlation with the wind friction velocity. However, spectral values at higher wavenumbers (above 200 rad m^{-1}) are significantly higher than previous laboratory results. In the presence of surface films wave spectra may decrease by more than one order of magnitude at lower wind stresses. The dispersion characteristics of short waves vary markedly depending on the wavenumber, the wind stress, and the surface chemical condition. Some results in the presence of surface films at intermediate winds show much higher apparent phase speeds than the theoretical dispersion relation. This may be because of an enhanced near-surface current or because of the relative increase of wave energy that is phase-locked to longer steep gravity waves.

1. Introduction

It has been recognized that short wind waves (gravity–capillary waves) play important roles in various air–sea interaction processes, including air–sea momentum flux and air–sea gas transfer. While shorter wind waves support a significant part of the total wind stress (momentum flux from air to water), their contribution has been parameterized only empirically (e.g., Charnock 1955), without addressing the detailed physical mechanism of the momentum flux. As a result, our predictive capability of the effective ocean surface roughness (or the

drag coefficient) is still far from satisfactory. Recent laboratory studies have suggested that short wind waves are closely correlated with the air–sea gas transfer velocity of slightly soluble gases (Jähne et al. 1987; Hara et al. 1995), and several theories have been proposed to explain such observations (e.g., Csanady 1990). Yet the exact mechanism of the air–sea gas transfer, including the role of short wind waves, is still a matter of contention. In order to improve our understanding of the influences of short wind waves on air–sea interaction processes, it is vital to obtain accurate measurements of short wind waves in a wide range of field conditions.

Direct observations of short wind waves are also important for the practical applications of microwave radar remote sensing of the ocean. For example, the interpretation of synthetic aperture radar (SAR) images requires a precise knowledge of the interaction between short wind waves (scatterer of microwaves) and other environmental parameters in the atmosphere (e.g., atmospheric turbulence, momentum flux, heat flux), at the air–sea interface (e.g., surface waves, wave breaking, air–sea gas flux), and in the ocean (e.g., near-surface turbulence, near-surface currents, internal waves).

Past direct observations of short wind waves have been carried out mostly in laboratory wind–wave flumes. Ebuchi et al. (1987) investigated fine structures of wind wave surfaces, such as rhombic patterns of gravity–capillary waves and parasitic capillaries. Jähne and Riemer (1990) measured spatial structures of short wind waves in a large wind–wave flume using an imaging optical technique. Their results have shown that the dynamics of gravity–capillary waves is very different from that of gravity waves and depends on the wind stress and the wavenumber in a quite complex manner. Further refinements of laboratory studies have been made by Hwang et al. (1993) and Zhang (1995); the latter has identified various features of parasitic capillary waves formed on the downwind faces of gravity waves. A laboratory study by Hara et al. (1997) has focused on the dispersion characteristics of short wind waves. They have shown that a significant part of short wind wave energy may be phase-locked to steep gravity waves—that is, propagate at the phase speed of the gravity waves. They have also suggested that nonlinear wave interactions may enhance the level of short wind waves in particular oblique directions relative to the mean wind.

Although recent laboratory studies have enhanced our knowledge of short wind waves in laboratory settings, in situ observations are still scarce. A field study by Hara et al. (1994), carried out in fetch-limited water, has shown that short wind wave spectra at low wind stresses are significantly higher than laboratory observations. A recent field observation by Hwang et al. (1996), obtained on open ocean, also shows marked difference between field and laboratory results. They attribute the difference to naturally occurring wind fluctuation in field conditions.

Here, we present the results of two recent field experiments on short wind waves using a scanning laser slope gauge. The instrument is capable of resolving the spatiotemporal structure of wind waves in the range of wavenumbers between 50 and 800 rad m^{-1}, and frequencies up to the Nyquist frequency of 52.1 Hz. In section 2, the overviews of the field programs and experimental methods are explained. The results and interpretations are presented in section 3. Our results demonstrate a strong influence of surface films, resulting in large variability of short wind wave spectra in a coastal environment. Our data also confirm the difference between field and laboratory wave conditions at lower wind stresses. Detailed investigations of the dispersion characteristics and directional spreading of short wind waves are also made. Finally in section 4, our observations are summarized and their implications to future studies are discussed.

2. Experimental overview

a. High-resolution remote sensing experiment

The main experiment of the High-Resolution Remote Sensing Accelerated Research Initiative (Hi-Res II) took place in June of 1993 and was sponsored by the Office of Naval Research and Naval Research Laboratory. The principal objective of the initiative was to perform an in-depth study of the relationship between radar backscatter and atmospheric, surface, and subsurface processes. To determine these relations, a research catamaran was deployed as a means of obtaining in situ measurements of gravity–capillary waves (using a scanning laser slope gauge), dominant gravity waves (using a capacitive wave wire and a motion detection package), and subsurface currents (using a three-axis acoustic Doppler current meter). The catamaran was equipped with an electric motor and a remotely controlled rudder, and was towed from the starboard side (about two-thirds of the total ship length from the bow) of the R/V *Iselin*. Its position was maintained at a distance of about 20 m to the side of the ship in order to minimize wind blockage and operate outside of the ship's wake. The tow speed was mostly between 0.5 and 1 m s^{-1}. The wind speed and the wind stress were obtained on the catamaran and at the bow of the ship using sonic anemometers (Edson et al. 1998). The locations of the experiment were near the coast of Cape Hatteras, North Carolina, and are shown in Fig. 1 by two large circles. Both sites were located in the vicinity of the Gulf Stream north wall. Therefore, data were collected both over coastal water and over Sargasso Sea water.

b. Coastal ocean processes experiment

As part of the Coastal Ocean Processes (CoOP) program sponsored by the National Science Foundation, an experiment

was carried out in April–May of 1995 to investigate the role of various ocean surface processes on the air–sea gas exchange. The research catamaran was towed to the side of the R/V *New Horizon.* Measurements of gravity–capillary waves, dominant gravity waves, subsurface currents/turbulence, and surface chemical enrichment were made possible with the instrument array aboard the catamaran. The array included a set of six capacitive wave wires, a motion detection package, a three-axis acoustic Doppler current meter, a hot film anemometer, and a surface skimmer. The measurement of the wind speed and the wind stress were made using a sonic anemometer at the bow of the ship. The locations of the experiment were off the coast of California and are shown in Fig. 2. They included both sites with low surface chemical enrichment values shown by diamonds and sites with high and variable enrichment values shown by crosses. Higher values of surface chemical enrichment are indicative of higher concentrations of surfactant (N. M. Frew 1995, personal communication).

c. Wind stress measurements

Wind stress estimates were made using sonic anemometers mounted on the two research vessels and the catamaran. Direct covariance flux systems were deployed during the Hi-Res II experiment at 11.5 and 5.6 m above the mean sea surface aboard the R/V *Iselin* and the research catamaran, respectively. These measurements were corrected for platform motion as described by Edson et al. (1998) to compute the momentum and heat fluxes using the direct covariance (eddy correlation) method. Instrumentation to measure the mean temperature and humidity was included in both packages. These measurements were combined with the mean wind speed (relative to the water surface) to estimate the flux using the bulk aerodynamic method described by Fairall et al. (1996). The sonic anemometers were also used to compute dissipation estimates using the Kolmogorov relationship and spectral estimates in the inertial subrange (Kolmogorov 1941). The dissipation rates were used with the semiempirical functions found in Fairall and Edson (1994) to compute inertial-dissipation flux estimates.

A similar set of instrumentation was deployed at a height of 10 m on a bow mast aboard the R/V *New Horizon* during the CoOP experiment. Problems with the vertical accelerometers (required to correct for ship motion) prohibited direct covariance flux estimates. Therefore, the stress estimates used in this paper are derived from the bulk aerodynamic and inertial dissipation methods using the formulations described above.

d. Short wind wave measurements

The measurements of short wind waves were carried out using a scanning laser slope gauge developed by Bock and Hara (1995). The instrument was previously used in a field study (Hara et al. 1994) and a laboratory study (Hara et a1. 1997). The data analysis scheme and the error analysis have been discussed in detail in earlier papers and are not repeated here. In short, the instrument yields three-dimensional wavenumber–frequency slope spectra of short wind waves for wavenumbers between 50 and 800 rad m^{-1} and frequencies up to the Nyquist frequency of 52.1 Hz during the CoOP (wavenumbers up to 400 rad m^{-1} and the Nyquist frequency 18.9 Hz during the Hi-Res II). Because of instrumental noise and sidelobes associated with our data analysis scheme, results near zero frequency may be contaminated. Therefore, care has been taken when the results are integrated in frequency to calculate wavenumber slope spectra [see Hara et al. (1997) for details]. During the CoOP experiment, the data were further contaminated by the vibration of the instrument. Fortunately, the noise from the vibration was almost uniform in space (concentrated near-zero wavenumber) and did not affect the real wave signal for wavenumbers above 50 rad m^{-1}. Further error analyses are summarized in the appendix.

e. Definitions

Let us define a coordinate system such that the x axis is in the mean wind direction, the z axis is vertically upward measured from the mean water surface, and the y axis is defined according to the right-hand rule. We denote the surface elevation by $z = \zeta(x, y, t)$, and the surface slope by $\nabla\zeta = (\partial\zeta/\partial x, \partial\zeta/\partial y)$. The autocorrelation function of the surface slope is defined as

$$R(\xi, \eta, \tau) = \overline{\nabla\zeta(x, y, t)\cdot\nabla\zeta(x + \xi, y + \eta, t + \tau)}, \quad (1)$$

where the overbar indicates the time average. Then, the three-dimensional one-sided frequency–wavenumber slope spectrum is calculated to be

$$S(k, \theta, \omega) = \frac{1}{4\pi^3}\int\int\int_{-\infty}^{\infty} R(\xi, \eta, \tau)e^{-i(k\xi\cos\theta + k\eta\sin\theta - \omega\tau)}\,d\xi\,d\eta\,d\tau, \quad (2)$$

where k is the wavenumber, ω is the angular frequency, and θ is the wave direction measured from the x axis in the counterclockwise direction. Here $\theta = 0$ corresponds to waves in the wind direction and $\theta = \pm\pi/2$ corresponds to waves in the crosswind directions. This three-dimensional spectrum is defined for $0 < k < \infty$, $-\infty < \omega < \infty$, and $-\pi/2 < \theta < \pi/2$. Note that a negative ω corresponds to waves propagating against the wind. By definition, the mean square slope is recovered by integrating $S(k, \theta, \omega)$ as

$$\overline{\nabla\zeta\cdot\nabla\zeta} = \int_{-\infty}^{\infty}\int_{-\pi/2}^{\pi/2}\int_{0}^{\infty} S(k,\ \theta,\ \omega)k\ dk\ d\theta\ d\omega. \quad (3)$$

The one-sided two-dimensional wavenumber spectrum is calculated by integrating $S(k, \theta, \omega)$ in frequency:

$$S(k,\ \theta) = \int_{-\infty}^{\infty} S(k,\ \theta,\ \omega)\ d\omega, \quad (4)$$

which is defined for $0 < k < \infty$ and $-\pi/2 < \theta < \pi/2$. The nondimensional degree of saturation is defined as

$$B(k,\ \theta) = k^2 S(k,\ \theta). \quad (5)$$

Finally, the omnidirectional (one-dimensional) wavenumber slope spectrum and the omnidirectional degree of saturation are defined as

$$S(k) = \int_{-\pi/2}^{\pi/2} S(k,\ \theta)\ d\theta \quad (6)$$

and

$$B(k) = k^2 S(k). \quad (7)$$

respectively.

3. Results and discussion

a. Wavenumber slope spectrum from current and past studies

We first summarize the results of the wavenumber slope spectrum from this study as well as from past studies. In Figs. 3–6 the omnidirectional degree of saturation, $B(k)$, is plotted against the wind friction velocity, u_*, from the bulk aerodynamic method, at four different wavenumbers k = 100, 200, 400, and 800 rad m^{-1}. Our results from the Hi-Res II and the CoOP experiments are shown by triangles and crosses, respectively. These results are averaged over 8 min so that the statistical scatter is negligibly small (Bock and Hara 1995). Therefore, the scatter in these figures must be due to real environmental variabilities. In addition to the results of this study, the figures contain data from two previous field studies. The results by Hara et al. (1994) (diamonds) were obtained at Martha's Vineyard Sound, Massachusetts, in November 1993. The wind fetch at the experimental location was limited to 7 km. The results of Hwang et al. (1996), shown as pairs of triangles connected vertically, were obtained during the same Hi-Res II experiment but using a scanning laser slope gauge of a very different design. Since they report the degree of saturation in the along-wind direction only, $B(k, \theta = 0)$, the omnidirectional value, $B(k)$, is estimated assuming two extreme directional spreading functions and are shown as upper and lower bounds. The upper bound corresponds to a uniform directional spreading, and the lower bound corresponds to a directional spreading of the form of $\cos\theta$. We have ascertained that most of the data from this study exhibit directional spreading, which falls between these two extreme spreading functions. Since our data from the Hi-Res II, shown by triangles, were obtained roughly at the same sites and at the same periods as those by Hwang et al. (1996), the reasonable agreement between the two datasets confirms the accuracy of both measurements. The laboratory results by Jähne and Riemer (1990), Zhang (1995), and Hara et al. (1997) were obtained at the fetch of roughly 100 m, 25 m, and 13 m, respectively. Since results with shorter fetches and at smaller wavenumbers are strongly fetch-dependent, such results are excluded from the figures.

At the lowest wavenumber k = 100 rad m^{-1}, most of the field results collapse rather tightly above u_* = 0.07 m s^{-1}, except some lower points from the Hi-Res II and the CoOP. The field results increase slowly and smoothly with wind stress. Although the laboratory results by Jähne and Riemer (1990) show two distinctive ranges, that is, $B(k)$ is constant below u_* = 0.3 m s^{-1} and increases with u_* above u_* = 0.3 m s^{-1}, their results fall within the scatter of the field results.

As the wavenumber increases to k = 200–800 rad m^{-1}, a well-defined cluster of the field results is still observed near the upper edge of the overall distribution in each figure. However, the location of the cluster deviates upward from the laboratory results as k increases. At k = 200 and 400 rad m^{-1}, the discrepancy between the cluster and the laboratory result by Jähne and Riemer (1990) is large at lower wind stresses but decreases at higher wind stresses. At k = 800 rad m^{-1}, the cluster is higher than the laboratory result by roughly one order of magnitude throughout the entire wind stress range. At wavenumbers k = 200–800 rad m^{-1}, we also observe a larger scatter of field results below the cluster at lower wind stresses. Some points are lower than those in the cluster by more than one order of magnitude.

b. Variability of slope spectrum from CoOP

To investigate the reason for the large scatter of the field data at higher wavenumbers and at lower wind stresses, we focus on the results at k = 400 rad m^{-1} from the CoOP experiment only. In Fig. 7 we plot the same omnidirectional degree of saturation, $B(k)$, separated by the location of the measurement. The diamonds correspond to data obtained on the western side of St. Catalina Island, shown by diamonds in Fig. 2. The environmental conditions there are characterized by large to unlimited fetches, very low values of surface chemical enrichment suggesting clean water surfaces, and well-developed swells. The crosses are data collected on the eastern side of St. Catalina Island or near St. Rosa Island, shown by crosses in Fig. 2. These locations are characterized by limited fetches, high and variable surface enrichment values indicating the presence of surface films, and very low swells. It is clear that the diamonds show a well-defined correlation with the wind friction velocity. On the other hand, the crosses scatter widely and are lower than the diamonds for the friction velocity below 0.25 m s^{-1}. As the wind stress increases, the higher values of the crosses approach those of the diamonds. At high winds ($u*$ > 0.25 m s^{-1}), the crosses seem to be smoothly connected to the diamonds at lower winds. These observations suggest that short wind waves on clean water surfaces show a well-defined correlation with the wind stress and those on water surfaces with surfactant are highly variable and generally lower than clear water results at lower winds ($u*$ < 0.25 m s^{-1}). At higher winds the effect of surfactant seems to become insignificant. It is also possible that the difference in fetch and swell conditions may contribute to the variability of short wind wave spectra.

In Fig. 8, we show the omnidirectional degree of saturation, $B(k)$, against the wavenumber, k, near three different wind friction velocities of $u*$ = 0.1, 0.2, and 0.3 m s^{-1}. Except for the cases with surfactant (the lower three lines near $u*$ = 0.2 m s^{-1} and the lower seven lines near $u*$ = 0.1 m s^{-1}), the degree of saturation is quite uniform over the range of wavenumbers shown. At lower wavenumbers $B(k)$ depends on $u*$ very weakly, while $B(k)$ increases slowly with $u*$ at higher wavenumbers. With surfactant, the results near $u*$ = 0.2 m s^{-1} gradually deviate from the clean water results between k = 100 and 400 rad m^{-1}. At higher wavenumbers the ratio between clean and surfactant cases seem to be almost constant. The results near $u*$ = 0.1 m s^{-1} in the presence of surfactant show that some $B(k)$ values are lower than the clean water values, even at low wavenumbers (k < 100 rad m^{-1}). The difference increases rapidly between k = 100 and 300 rad m^{-1}. Above k = 300 rad m^{-1}, $B(k)$ is as small as 2% of the clean water values.

It is rather surprising that at $u*$ = 0.3 m s^{-1} the degree of saturation increases rapidly (almost linearly) with k and reaches as high as 0.07 at k = 800 rad m^{-1}. These results also look anomalously high in Fig. 6. However, our error analyses (see appendix) suggest that there are no significant error sources that may artificially increase the spectral estimate. It is of interest to see whether future wind wave measurements by other methods will yield similar high values in open ocean conditions.

c. Difference between field and laboratory results

As we have discussed in the previous subsection, lower values of the field results are probably attributable to the presence of surface films. Then, the major cluster of the field results near the upper edge in Figs. 3–6 can be considered as typical field values at clean water surfaces. However, this does not explain the large discrepancy between the field results and the laboratory results in these figures. Such discrepancy was also reported by Hwang et al. (1996). One might be tempted to suspect that the previous laboratory results were always contaminated by surface films. However, during the laboratory experiment reported by Hara et al. (1997), surface chemical conditions were carefully monitored and were found to be very clean. Mechanically generated capillary waves were found to dissipate at the predicted dissipation rate, and the measured surface tension was consistent with the clean water value. Furthermore, the reasonable agreement between the results by Hara et al. (1997) and those by Jähne and Riemer (1990) at higher wavenumbers suggests that the experiment by Jähne and Riemer (1990) was also conducted with clean water surfaces (the deviation at lower wavenumbers can be attributed to differences in fetch). Therefore, we need to provide different explanations for the discrepancy between laboratory and field results.

One possible reason is the influence of wind fluctuation as suggested by Hwang et al. (1996). The fluctuation of the wind friction velocity is always much larger in the field than in laboratories. Since the laboratory results of $B(k)$ increase faster than linearly with $u*$ at higher wavenumbers, a larger fluctuation of $u*$ may increase the mean value of $B(k)$ for a given mean $u*$, if the statistical distribution of $u*$ values is symmetric above and below its mean. However, this bias due to wind fluctuation is not likely to account for the tenfold increase of $B(k)$ from laboratories to the field. Another possible reason for the higher short wind wave spectra in the field is the influence of nonlinear interactions among different wave modes. These may include the interaction among three or more free-propagating waves that satisfy the resonance condition. Evidences of such wave interactions have been reported by Zhang (1995) and Hara et al. (1997) in laboratory settings. In addition, observations by Hara et al. suggest a possibility that interactions take place among two symmetric oblique short waves and longer steep gravity waves when the sum frequency and the sum wavenumber vector of the two oblique modes match those of one of the higher harmonics of the gravity waves. Alternatively, this mechanism might be considered as small-scale short-crested roughness excited by, and phase-locked to, steep gravity waves. If longer gravity waves play an important role in exciting short waves, the difference between the field and laboratories can be attributed, at least in part, to the difference of gravity wave fields.

d. Frequency–wavenumber slope spectrum

In this section we examine the dispersion characteristics of short wind waves through their frequency–wavenumber spectrum obtained during the CoOP. We first remove the Doppler shift due to the tow speed of the catamaran, using the mean relative current measured by a shipboard acoustic Doppler current profiler (ADCP) and averaged over eight minutes. During limited deployments, collocated simultaneous mean current measurements were made at a 0.2-m depth using the acoustic current meter mounted on the catamaran. We have ascertained that the difference between the two current measurements is less than 10% of the ADCP current values (typically 0.5–1.0 m s^{-1}) in most cases. The results are still influenced by the Doppler shifts due to gravity wave orbital velocities and due to the fluctuation of the tow speed that depends on the dynamical response of the catamaran to the gravity wave motion. It has been found that, when large swells are present, the responding motion of the towed catamaran introduces a large Doppler shift that masks most of the dispersion characteristics of short waves. Therefore, we only present results obtained without significant swells—that is, cases corresponding to crosses in Fig. 7. We do not show the results at lower wavenumbers (k < 50 rad m^{-1}) because the data are contaminated by the instrument vibration.

In Figs. 9 and 10, we show the three-dimensional wavenumber–frequency slope spectrum $S(k, \theta, \omega)$ along the mean wind direction $\theta = 0$. The same slope spectra at two fixed wavenumbers, k = 150 and 300 rad m^{-1}, but in all directions are shown in Figs. 11 and 12. Note that the scale is relative and exaggerated in Figs. 11 and 12. These two sets of data were obtained 78-min apart during the same catamaran deployment, and correspond to the two large circles in Fig. 7. Although the wind stress remained almost constant over the period ($u*$ = 0.24 m s^{-1} for both figures), the degree of saturation at k = 400 rad m^{-1} decreased by a factor of 4, corresponding to increasing surface enrichment values (indicative of increasing surface films). In these figures solid lines are added to indicate the theoretical dispersion relation of gravity–capillary waves:

$$\omega^2 = gk + \frac{\gamma k^3}{\rho}, \qquad (8)$$

where g is the gravitational acceleration, γ is the surface tension (γ = 0.073 N m^{-2} is used), and ρ is the density of water. The positive and negative solutions of (8) correspond to the waves propagating in the wind direction (alongwind waves) and those propagating against the wind, respectively.

In Figs. 9 and 11, the peak of the spectrum is located slightly below the dispersion relation of alongwind waves (upper solid line), and the wave energy spreads widely in frequency above and below the peak. Relatively high spectral values are observed at negative frequencies corresponding to waves (apparently) propagating against the wind. These observed spectra cannot be attributed solely to alongwind gravity–capillary waves that are Doppler shifted by longer gravity waves. Although large negative orbital velocities of longer gravity waves can temporarily Doppler shift the spectrum into negative frequencies, they cannot shift the entire spectrum in the negative direction, as in Figs. 9 and 11, unless most of the short wind waves are concentrated near the troughs of the longer gravity waves, which is not likely. It is possible that the entire spectrum is shifted to lower frequencies by a strong adverse near-surface mean current. However, there are no reasonable physical explanations why a near-surface current may develop against the wind relative to the bulk current measured by the ADCP. We therefore suspect that some of the short waves are literally propagating against the wind. With our limited observations we cannot completely rule out a possibility that upwind-traveling waves were generated by the towed platform itself. Further observational studies are needed to clarify the source of the upwind-traveling waves. The directional spreading of the wave energy becomes more uniform as the wavenumber increases. The slope spectrum of the crosswind waves is lower than that of alongwind waves by 25%–30% at k = 150 rad m^{-1} and by 15%–20% at k = 300 rad

m^{-1} if integrated over all frequencies.

After 78 min the slope spectrum decreases significantly at higher wavenumbers. At the same time, the dispersion characteristics change as is shown in Fig. 10. Now the wave energy is distributed more narrowly in frequency indicating less Doppler shifting. The phase speed of the waves is much larger than the previous results and is high above the theoretical dispersion relation shown by the upper solid line. There is no appreciable wave energy in negative frequencies. The directional frequency spectra in Fig. 12 also differ from those in Fig. 11. At k = 150 rad m^{-1} the spectral level (integrated in all frequencies) in the crosswind direction is lower than that in the alongwind direction by 15%–20%; that is, the directional spreading is more uniform than in Fig. 11a. At the higher wavenumber of k = 300 rad m^{-1}, the crosswind value is 25%–30% lower than the peak value—that is, the distribution is more peaked than in Fig. 11b.

One possible explanation of the large change of the dispersion characteristics from Fig. 9 to Fig. 10 is that a strong near-surface current developed over the 78-min period. If we add a near-surface current of 0.27 m s^{-1} in the wind direction relative to the bulk current measured by the ADCP, the theoretical dispersion relation is shifted to the dotted lines in Figs. 10 and 12 and becomes quite consistent with the observed wave spectrum. Here, the Doppler-shifted frequency ω_D is given as

$$\omega_D = \omega + uk\cos\theta, \quad (9)$$

where u is the assumed near-surface current velocity and ω is given by (8). This explanation, however, does not provide the reason why the waves propagating against the wind are preferentially damped by surface films, nor the reason why the Doppler shift by longer gravity waves of alongwind waves is reduced in the presence of surface films (since longer gravity waves are not expected to be influenced by surface films). Note that a possible change of the dispersion relation due to a modified surface tension (γ) by surface films is negligibly small compared to the Doppler shift of this magnitude.

An alternative explanation is that the short wind waves in Figs. 10 and 12 are not propagating freely but are bound to steep gravity waves. Then the shorter waves in the wind direction (i.e., the higher harmonics of the gravity waves) should appear to propagate at the same phase speed as the steep gravity waves rather than at their own phase speeds. Furthermore, if there is short-crested (i.e., two-dimensional) small-scale surface roughness that propagates with the gravity waves, its frequency–wavenumber spectrum should be concentrated near the apparent frequency of

$$\omega_B = kC\cos\theta, \quad (10)$$

where C is the phase speed of the gravity waves. In Figs. 10 and 12, we have added ω_B (dashed lines) for a chosen phase speed of C = 0.45 m s^{-1} that corresponds to gravity waves of k = 49 rad m^{-1} or the wavelength of 0.13 m. The observed spectrum seems to follow the dashed lines as closely as it follows the dotted lines. Therefore, it may be interpreted that surface films have almost eliminated freely propagating shorter wind waves and that only the higher harmonics of steep gravity waves are measurable. This explanation is also consistent with the disappearance of the waves propagating against the wind and the reduction of the Doppler shift of alongwind waves. Note that the spectral level in Fig. 9 is higher everywhere in the k–ω plane than that in Fig. 10. Therefore, it is possible that the higher harmonics of steep gravity waves are also present in Fig. 9 but are concealed by much higher freely propagating waves.

One weakness of the second explanation is that there are no obvious reasons why a single component of gravity waves near k = 49 rad m^{-1} has to be so dominant in Fig. 10. The comparison of the integrated wavenumber slope spectra of both cases indicates that k = 49 rad m^{-1} roughly corresponds to a threshold wavenumber above which the spectrum is reduced by surface films (the spectral values corresponding to Fig. 10 are 98%, 69%, and 33% of those corresponding to Fig. 9 at wavenumbers 50, 100, and 200 rad m^{-1}, respectively). While this may explain why we do not see any bound harmonics of gravity waves above k = 49 rad m^{-1}, it is still not clear why no bound harmonics of longer gravity waves are observed.

In our recent laboratory studies of wind waves reported by Hara et al. (1997), we have found that a significant part of shortwave energy may be bound to dominant gravity waves in the wind–wave flume, depending on the wind and fetch conditions. Although simple extrapolations of laboratory results to field conditions cannot be made, it is noteworthy that certain common dispersion characteristics of short wind waves are observed both in laboratory studies and in field observations. Of course, without further independent physical measurements to augment these observations, we cannot reject the first explanation nor justify the second explanation.

At lower wind stresses between 0.15 and 0.25 m s^{-1} and with varying surface chemical enrichment levels, we have observed similar transitions of wave spectra between those characterized by broader Doppler shifting and significant levels

of waves at negative frequencies such as Figs. 9 and 11 and those characterized by narrower Doppler shifting, negligible spectral levels at negative frequencies, and larger phase speeds than the theoretical dispersion relation such as Figs. 10 and 12. At very low wind stresses, however, wave spectra seem to follow the theoretical dispersion relation even in the presence of surface films. Such an example is shown in Fig. 13, which corresponds to the large square in Fig. 7. This may be simply due to the disappearance of the near-surface drift current, or because the longer gravity waves are not steep enough to generate higher bound harmonics at such low winds.

e. Directional wavenumber spectrum

Another way to observe the wave characteristics is to integrate the three-dimensional spectrum in frequency to obtain the two-dimensional (directional) wavenumber slope spectrum $S(k, \theta)$ or the directional degree of saturation $B(k, \theta)$. In Figs. 14 and 15, $B(k, \theta)$ is shown for the two cases corresponding to Figs. 9 and 10, respectively. At an earlier stage (Fig. 14), the directional spreading is quite uniform at higher wavenumbers. After 78 min in Fig. 15, shorter wind waves ($k > 300$ rad m^{-1}) show a more distinctive peak along the wind direction, and the crosswind values are lower than the alongwind values by roughly 30%–40%. On the other hand, at lower wavenumbers ($k < 200$ rad m^{-1}) the directional spreading is quite broad. These are consistent with Figs. 11 and 12. The result at a very low wind friction velocity in Fig. 16 (corresponding to Fig. 13 and the large square in Fig. 7) shows a clear peak along the wind direction for the entire wavenumber range up to $k = 400$ rad m^{-1}, beyond which the wave signal becomes too noisy to resolve its directionality. On the other hand, the result at a similar low wind friction velocity but over a clean water surface in Fig. 17 (corresponding to the big triangle in Fig. 7) shows more uniform directional spreading.

4. Concluding remarks

Field observations have been made of wind-generated gravity–capillary waves during the Hi-Res II and the CoOP programs. Our results of short wind wave spectra over clean water compare reasonably with past field observations and show much higher values than laboratory results at lower winds and at higher wavenumbers. The results also show large variability in the presence of surface films; some results are lower than clean water values by more than one order of magnitude at higher wavenumbers. Our detailed investigations of the wavenumber–frequency spectra of short wind waves show that the dispersion characteristics vary significantly depending on the wavenumber, the wind stress, and the surface chemical conditions. On clean water, a significant part of the wave energy seems to belong to waves propagating against the wind. The apparent phase speed of short wind waves may increase in the presence of surface films, either by the enhancement of near-surface currents or by the relative increase of the wave energy that is bound to steep gravity waves.

With our limited observations, many questions remain unanswered. The large discrepancy between laboratory and field conditions does not seem to be attributable to the wind-fluctuation alone. Interactions between gravity–capillary waves and longer gravity waves may play an important role in determining the level of the slope spectrum. Although some of our observations may be suggestive of such interactions, they are far from comprehensive to draw any conclusions. Further progress on these issues may require simultaneous observations of waves in wide spatial and temporal ranges including capillary, gravity–capillary, and gravity waves. Many of our observations indicate that the dynamics of short wind waves are significantly nonlinear. Therefore, higher-order data analyses that explicitly account for the nonlinearity may be desirable.

Our observations imply that use of laboratory results requires much care for the study of air–sea interaction processes and for the application to microwave radar remote sensing. The large variability of short wind waves in coastal environments suggests the importance of surface chemistry in the study of small-scale air–sea interaction processes.

Acknowledgments

We thank Dr. Nelson M. Frew for providing surface film information, and Mr. B. Mete Uz for his assistance in spectral calculations. We also thank two anonymous reviewers for their helpful comments. This research was supported by NSF Grants OCE-9409222 (TH) and OCE-9410537 (EJB, JBE) and ONR Grants N00014-95-1-0116, N00014-96-1-0510 (TH), and N00014-90-J-1717, N00014-96-0516 (EJB, JBE).

REFERENCES

Bock, E. J., and T. Hara, 1995: Optical measurements of capillary–gravity wave spectra using a scanning laser slope gauge. *J. Atmos. Oceanic Technol.*, **12,** 395–403..

Charnock, H., 1955: Wind stress on a water surface. *Quart. J. Roy. Meteor. Soc.*, **81,** 639..

Csanady, G. T., 1990: The role of breaking wavelets in air–sea gas-transfer. *J. Geophys. Res.*, **95,** 749–759..

Ebuchi N., H. Kawamura, and Y. Toba, 1987: Fine structure of laboratory wind–wave surfaces studied using an optical method. *Bound.-Layer Meteor.*, **39,** 133–151..

Edson, J. B., J. E. Hare, and C. W. Fairall, 1998: Direct covariance flux estimates from mobile platforms at sea. *J. Atmos. Oceanic Technol.*, **15,** 547–562..

Fairall, C. W., and J. B. Edson, 1994: Recent measurements of the dimensionless turbulent kinetic energy dissipation function over the ocean. Preprints, *Second Int. Conf. on Air–Sea Interaction and on Meteorology and Oceanography of the Coastal Zone*, Lisbon, Portugal, Amer. Meteor. Soc., 224–225..

— ,E. F. Bradley, D. P. Rodgers, J. B. Edson, and G. S. Young, 1996: Bulk parameterization of air–sea fluxes for Tropical Ocean Global Atmosphere Coupled Ocean–Atmosphere Response Experiment. *J. Geophys. Res.*, **101,** 3747–3764..

Hara, T., E. J. Bock, and D. Lyzenga, 1994: In situ measurements of capillary–gravity wave spectra using a scanning laser slope gauge and microwave radars. *J. Geophys, Res.*, **99,** 12 593–12 602..

— ,— ,N. M. Frew, and W. R. McGillis, 1995: Relationship between air–sea gas transfer velocity and surface roughness. *Air–Water Gas Transfer*, B. Jähne and E. C. Monahan, Eds., AEON Verlag, 611–616..

— ,— ,and M. Donelan, 1997: Frequency–wavenumber spectrum of wind-generated gravity-capillary waves. *J. Geophys, Res.*, **102,** 1061–1072..

Hwang, P. A., D. B. Trizna, and J. Wu, 1993: Spatial measurements of short wind waves using a scanning slope sensor. *Dyn. Atmos. Oceans*, **20,** 1–23..

— ,S. Atakturk, M. A. Sletten, and D. B. Trizna, 1996: A study of the wavenumber spectra of short water waves in the ocean. *J. Phys. Oceanogr.*, **26,** 1266–1285..

Jähne, B. K., and K. S. Riemer, 1990: Two-dimensional wave number spectra of small-scale water surface waves. *J. Geophys. Res.*, **95,** 11 531–11 546..

— ,O. Münnich, R. Bösinger, A. Dutzi, W. Huber, and P. Libner, 1987: On the parameters influencing air–water gas exchange. *J. Geophys. Res.*, **92,** 1937–1949..

Kolmogorov, A. N., 1941: Energy dissipation in locally isotropic turbulence. *Dokl. AN SSSR*, **32,** 19–21..

Zhang, X., 1995: Capillary–gravity and capillary waves generated in a wind wave tank: Observations and theories. *J. Fluid Mech.*, **289,** 51–82..

APPENDIX

5. Error Analysis

Here, we summarize the error analyses of the scanning laser slope gauge. We have identified six possible sources of errors in Bock and Hara (1995); these are bias due to pitch/roll of the instrument, bias due to calibration, effect of a finite scan speed, statistical random errors, data dropouts, and numerical sidelobes. Here, we focus on the last two sources, since the first four are expected to be very small (less than ±1 dB).

a. Data dropouts

Data dropouts occur for two reasons: one being locally large surface slope that is outside the resolvable range of the instrument and the other being large gravity waves that yield water surface levels either below the top of the laser pod or above the bottom of the head unit.

The maximum resolvable surface slope is between 0.62 and 2.41, depending on the direction of the surface slope and the location of the laser beam. The most conservative estimate of the data dropout rate would be the probability of the surface slope exceeding 0.62. We have found that this probability is 2.9% and that the actual observed data dropout rate is only 0.7% at the friction velocity of $u_* = 0.3$ m s^{-1}. Therefore, this is not likely to be a major source of errors in the slope spectral estimate.

Data dropouts due to large gravity waves can be easily identified since the surface slope becomes either unmeasurable (when the top of the laser pod is above water) or zero (when the bottom of the head unit is below water). In order to avoid any possible data contaminations, we discard data for several seconds after each dropout. At the friction velocity $u_* = 0.3$ m s^{-1}, up to 50% of the data are discarded for this reason. It is possible that a high data dropout rate may bias the spectral estimate if dropouts occur at a particular phase of long waves and the spectral calculation excludes the gravity–capillary wave information from the vicinity of the particular phase of the long waves. Our visual observations, however, indicate that dropouts occur erratically because of the complicated dynamical response of the towed catamaran to waves. Therefore, we do not suspect that data dropouts due to large gravity waves introduce any significant bias to the spectral estimate.

b. Numerical sidelobes

The estimated two-dimensional wavenumber slope spectrum $\hat{S}(\mathbf{k})$ is a convolution integral of the real spectrum $S(\mathbf{k})$ and a convolution function $R(\mathbf{k})$ centered around the wavenumber of interest:

$$\hat{S}(\mathbf{k}) = \int_{-\infty}^{\infty}\int_{-\infty}^{\infty} S(\mathbf{k}')R(\mathbf{k}' - \mathbf{k})\, d\mathbf{k}'. \qquad \text{(A1)}$$

The shape of the convolution function R is determined by the spatial sampling rate and a chosen windowing function. In our spectral calculation, the convolution function has a narrow sharp peak at the origin and decreases rapidly away from the origin to about 10^{-4} relative to the peak, but increases again near the radius of 2000 rad m^{-1}. For example, the spectral estimate at $k = 800$ rad m^{-1} in the wind direction can be affected by waves at $k = 2800$ rad m^{-1} in the wind direction, at $k = 1833$ rad m^{-1} in the cross-wind directions, or at $k = 1200$ rad m^{-1} in the direction opposite to the wind. These effects are comparable to the aliasing (spectral foldover) in one-dimensional spectral analyses. In addition, the spectral estimate can be affected by waves near $k = 0$ rad m^{-1}, if the spectral level there is higher than that at $k = 800$ rad m^{-1} by more than four decades. It has been found that the leakage from the spectrum near $k = 0$ rad m^{-1} is so serious in field conditions that it sets a practical upper limit of the wavenumber resolution to be 800 rad m^{-1}. On the other hand, the aliasing from higher wavenumbers are expected to be small at this wavenumber since the slope spectrum always falls faster than k^{-1}.

c. Platform effect

In addition to the errors associated with the instrument, the platform (catamaran) may introduce systematic errors by disturbing the wind field, the wave field, and/or the near-surface current field. Although it is very difficult to quantify such effects, our visual observations suggest that the platform does not influence the wind–wave field as long as the catamaran is towed into the wind.

Figures

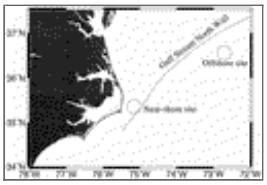

Click on thumbnail for full-sized image.

Fig. 1. Location of High-Resolution Remote Sensing Main Experiment (Hi-Res II).

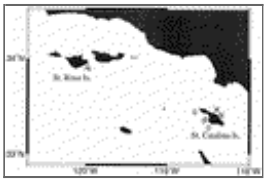

Click on thumbnail for full-sized image.

Fig. 2. Location of Coastal Ocean Processes Experiment (CoOP). Crosses, sites with high and variable surface enrichment values. Diamonds, sites with low surface enrichment values.

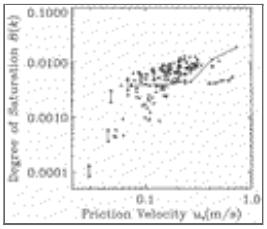

Click on thumbnail for full-sized image.

Fig. 3. Omnidirectional degree of saturation vs wind friction velocity at wavenumber 100 rad m^{-1}. Crosses: this study (CoOP); triangles: this study (Hi-Res II); pairs of triangles connected vertically by solid lines: Hwang et al. (1996); diamonds: Hara et al. (1994); crosses connected by solid lines: Jähne and Riemer (1990); and squares connected by solid lines: Zhang (1995).

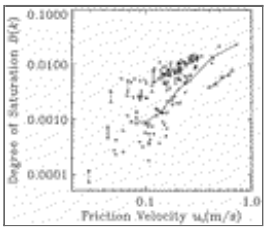

Click on thumbnail for full-sized image.

Fig. 4. Omnidirectional degree of saturation vs wind friction velocity at wavenumber 200 rad m^{-1}. Crosses: this study (CoOP); triangles: this study (Hi-Res II); pairs of triangles connected vertically by solid lines: Hwang et al. (1996); diamonds: Hara et al. (1994); crosses connected by solid lines: Jähne and Riemer (1990); squares connected by solid lines: Zhang (1995)

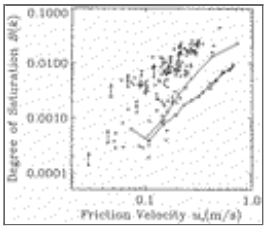

Click on thumbnail for full-sized image.

Fig. 5. Omnidirectional degree of saturation vs wind friction velocity at wavenumber 400 rad m^{-1}. Crosses: this study (CoOP); triangles: this study (Hi-Res II); pairs of triangles connected vertically by solid lines: Hwang et al. (1996); diamonds: Hara et al. (1994); crosses connected by solid lines: Jähne and Riemer (1990); squares connected by solid lines: Zhang (1995); diamonds connected by solid lines: Hara et al. (1997).

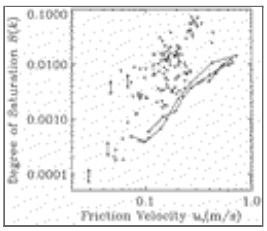

Click on thumbnail for full-sized image.

Fig. 6. Omnidirectional degree of saturation vs wind friction velocity at wavenumber 800 rad m^{-1}. Crosses: this study (CoOP); pairs of triangles connected vertically by solid lines: Hwang et al. (1996);diamonds: Hara et al. (1994); crosses connected by solid lines: Jähne and Riemer (1990); squares connected by solid lines: Zhang (1995);diamonds connected by solid lines: Hara et al. (1997).

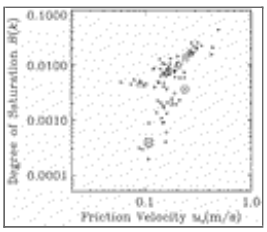

Click on thumbnail for full-sized image.

Fig. 7. Omnidirectional degree of saturation vs wind friction velocity at wavenumber 400 rad m^{-1} from CoOP. Crosses: sites with high and variable surface enrichment values; diamonds: sites with low surface enrichment values. Large symbols correspond to cases discussed in detail in the text.

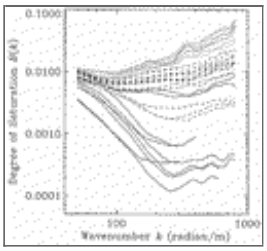

Click on thumbnail for full-sized image.

Fig. 8. Omnidirectional degree of saturation vs wavenumber. Dotted lines: near $u_* = 0.3$ m s^{-1}; dashed lines: near $u_* = 0.2$ m s^{-1}; solid lines: near $u_* = 0\ 1$ m s^{-1}.

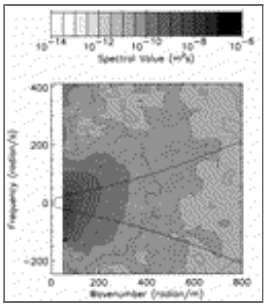

Click on thumbnail for full-sized image.

Fig. 9. Three-dimensional wavenumber–frequency slope spectrum corresponding to upper large circle in Fig. 7 for alongwind direction. Here $u_* = 0.24$ m s^{-1}. Solid line: dispersion relation. Contours are at every 2.5 dB.

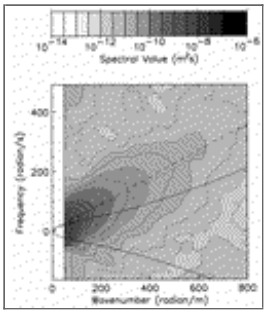

Click on thumbnail for full-sized image.

Fig. 10. Three-dimensional wavenumber–frequency slope spectrum corresponding to lower large circle in Fig. 7 for alongwind direction. Here $u_* = 0.24$ m s^{-1}. Solid line: dispersion relation; dotted line: dispersion relation with surface drift 0.27 m s^{-1}; dashed line: phase speed of gravity waves of $k = 49$ rad m^{-1}. Contours are at every 2.5 dB.

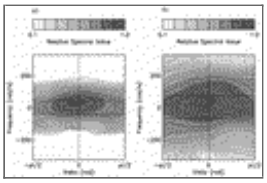

Click on thumbnail for full-sized image.

Fig. 11. Three-dimensional directional frequency slope spectrum (relative to maximum) corresponding to upper large circle in Fig. 7 for (a) $k = 150$ rad m^{-1} and (b) $k = 300$ rad m^{-1}. Here $u_* = 0.24$ m s^{-1}. Solid line: dispersion relation. Contours are at every 0.625 dB.

Click on thumbnail for full-sized image.

Fig. 12. Three-dimensional directional frequency slope spectrum (relative to maximum) corresponding to lower large circle in Fig. 7 for (a) k = 150 rad m^{-1} and (b) k = 300 rad m^{-1}. Here $u_* = 0.24$ m s^{-1}. Solid line: dispersion relation; dotted line: dispersion relation with surface drift 0.27 m s^{-1}; dashed line: phase speed of gravity waves of k = 49 rad m^{-1}. Contours are at every 0.625 dB.

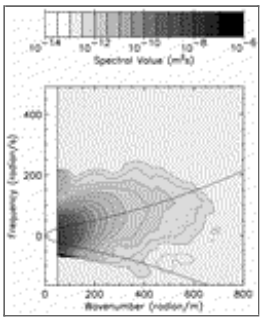

Click on thumbnail for full-sized image.

Fig. 13. Three-dimensional wavenumber–frequency slope spectrum corresponding to large square in Fig. 7 for alongwind direction. Here $u_* = 0.108$ m s^{-1}. Solid line: dispersion relation. Contours are at every 2.5 dB.

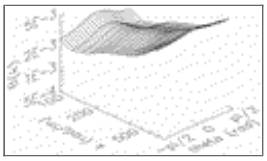

Click on thumbnail for full-sized image.

Fig. 14. Two-dimensional degree of saturation corresponding to upper large circle in Fig. 7. Here $u_* = 0.24$ m s^{-1}.

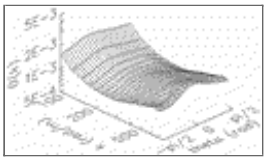

Click on thumbnail for full-sized image.

Fig. 15. Two-dimensional degree of saturation corresponding to lower large circle in Fig. 7. Here $u_* = 0.24$ m s^{-1}.

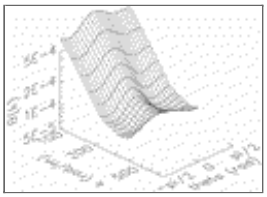

Click on thumbnail for full-sized image.

Fig. 16. Two-dimensional degree of saturation corresponding to large square in Fig. 7. Here $u_* = 0.108$ m s^{-1}.

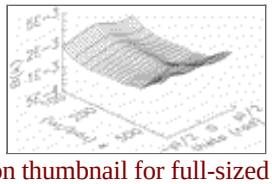

Click on thumbnail for full-sized image.

Fig. 17. Two-dimensional degree of saturation corresponding to large triangle in Fig. 7. Here $u_* = 0.090$ m s^{-1}.

* Woods Hole Oceanographic Institution Contribution No. 9562.

Corresponding author address: Dr. Tetsu Hara, Graduate School of Oceanography, University of Rhode Island, South Ferry Road, Narragansett, RI 02882.

E-mail: t.hara@gso.uri.edu

top